

# Tunable Photoelectric Properties of n-Type Semiconducting Polymer:Small Molecule Blends for Red Light Sensing Phototransistors

Chia-Chi Lin, Arulmozhi Velusamy, Shih-Huang Tung, Itaru Osaka, Ming-Chou Chen,\* and Cheng-Liang Liu\*

Semiconducting blend heterostructures, composed of conjugated polymer with photoresponsive organic crystals, provide an effective way to achieve promising photodetection devices. Here, solution-processed n-type N2200 conjugated polymer and quinoidal thienoisoindigo (TIIQ) small molecule blend is used to construct phototransistors for red light detection. The device performance of the optically switchable phototransistors can be tuned by the relative composition in the blend. The key feature is red light (680 nm) illuminated intensity-tunable photodetection enabling the highest photoresponsivity ( $R$ ) of  $4065 \text{ A W}^{-1}$  and specific photodetectivity ( $D^*$ ) of  $1.4 \times 10^{13}$  Jones for an 88% blend device. At the same time, maintaining high mobility ( $\mu$ ) of  $1.59 \text{ cm}^2 \text{ V}^{-1} \text{ s}^{-1}$ , since the efficient extraction of photogenerated charges from blend heterointerface, benefiting from blending with higher  $\mu$  and enhanced absorption of TIIQ, contributes to improvement in the red light photoresponse of the N2200:TIIQ blend phototransistor. This work demonstrates that the semiconducting blend strategies provide opportunities for developing high performance organic phototransistors.

## 1. Introduction

Optically active organic field effect transistors (or so-called organic phototransistors), in which optical functionalities are integrated in conventional field effect transistors, can realize the photoelectric conversion of the organic semiconductor materials.<sup>[1–9]</sup> Both organic single crystals<sup>[10]</sup> and conjugated polymers<sup>[11,12]</sup> are used as the organic-based photoactive materials in the phototransistors. The three-terminal organic phototransistor with low noise and electrical signal amplification usually has a bottom-gate type device architecture, since the photosensitive channel receives light from the top. The major merits of such devices are the wide range of light absorption for broadband photoresponse and the high responsivity of organic photoactive layer to light stimulation. High performance visible

wavelength-selective photodetection has been widely studied, especially for blue and green light, through changing the molecular design of photosensitive organic semiconductors to tune the wavelength of the absorbed light to the desired spectral range.<sup>[13–15]</sup> Far fewer red light photodetectors are reported, probably since the low bandgap organic compounds are typically more photosensitive to blue/green light and also meet the stability and solubility criteria.<sup>[4,16,17]</sup>

Photogenerated charge carriers (holes/electrons) of organic phototransistors, upon the absorption of incident photons, can be collected in the electrode under appropriate bias voltages, typically featuring a heterojunction between two conjugated organic semiconductors with different electronic affinity.<sup>[18,19]</sup> This thin heterojunction, consisting of electron donor and acceptor, either blended to form the bulk heterojunction or deposited sequentially to form the planar heterojunction, provides the energy offsets of the photoactive junction for effective separation of bonded excitons.<sup>[5,20–27]</sup> The interfacial charge effect between the separation, transport, and recombination is crucial for high photoresponse of organic phototransistors. Fullerene derivatives are dominantly selected as the electron acceptors, while many electron donors are available for photodetection layer assembling.<sup>[28–37]</sup> However, the fullerenes suffer from insufficient red light absorption, due to their wide

C.-C. Lin

Department of Chemical and Materials Engineering  
National Central University  
Taoyuan 32001, Taiwan

C.-C. Lin, I. Osaka

Applied Chemistry Program  
Graduate School of Advanced Science and Engineering  
Hiroshima University  
Higashi-Hiroshima, Hiroshima 739-8527, Japan

A. Velusamy, M.-C. Chen


Department of Chemistry  
National Central University  
Taoyuan 32001, Taiwan  
E-mail: mcchen@ncu.edu.tw

S.-H. Tung

Institute of Polymer Science and Engineering  
National Taiwan University  
Taipei 10617, Taiwan

C.-L. Liu

Department of Materials Science and Engineering  
National Taiwan University  
Taipei 10617, Taiwan  
E-mail: liucl@ntu.edu.tw

 The ORCID identification number(s) for the author(s) of this article can be found under <https://doi.org/10.1002/adom.202102650>.

DOI: 10.1002/adom.202102650

bandgap and morphological instability.<sup>[38,39]</sup> Nam et al. used the all-polymers bulk heterojunction layers consisting of electron-donating PTB7 and electron-withdrawing P(NDI2OD-T2) for an efficient red light sensing phototransistor with  $R$  as high as  $14 \text{ A W}^{-1}$  and better on/off switching characteristics,<sup>[40]</sup> where this blend offers strong red light absorption and efficient charge separation. In order to further enhance the device photoelectric properties, high carrier mobility for charge transfer, high optical sensitivity for exciton generation, and appropriate energy level alignment for increased charge separation efficiency of photoactive semiconducting blends used for red light sensing phototransistor are required.<sup>[41–43]</sup>

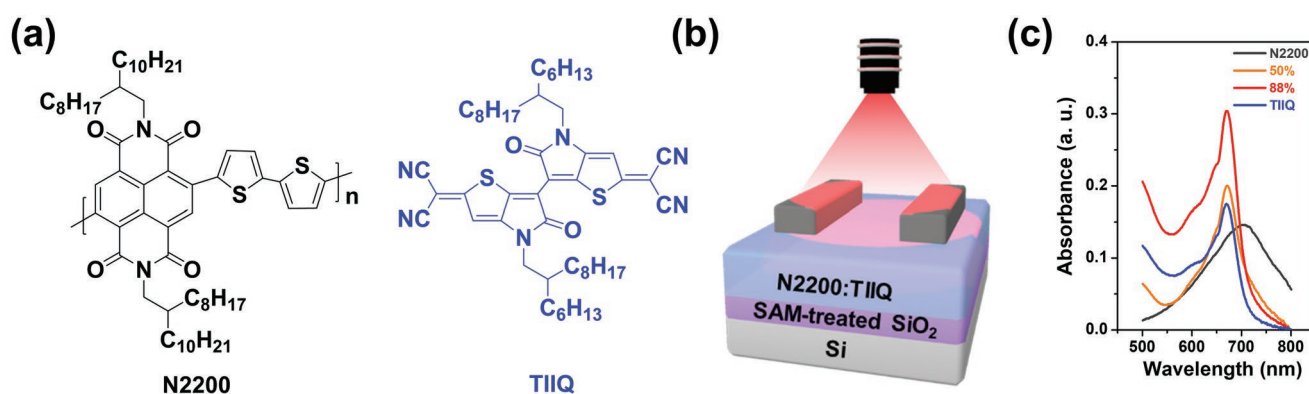
Starting from the n-channel red light absorbing N2200 (same structure as P(NDI2OD-T2)), our previously reported quinoindal thienoisindigo (TIIQ) small molecule semiconductors with high electron mobilities of  $>1 \text{ cm}^2 \text{ V}^{-1} \text{ s}^{-1}$  are introduced for phototransistors,<sup>[44]</sup> while constructing the enhanced absorption in the red light region and as-formed built-in electric field for photoexcited charge separation. Herein, we present the solution sheared deposition of pristine N2200 and TIIQ films and their blends (50% and 88% of TIIQ in blend layer) for optimizing the photoresponse of the red light (680 nm) sensing phototransistor. Under such an n-type N2200 polymer:TIIQ small molecule semiconducting blend circumstance, the corresponding photoresponsivity ( $R$ ) of  $4065 \text{ A W}^{-1}$  and specific photodetectivity ( $D^*$ ) of  $1.4 \times 10^{13}$  Jones of 88% N2200:TIIQ blend phototransistor are much higher than those of the pristine devices. Furthermore, key photoelectric parameters of our phototransistor, as compared with those of reported polymer blend-based devices from recent literature, are presented in Table S1, Supporting Information. The excellent performance of fabricated phototransistor is attributed to N2200:TIIQ blend heterointerface, which facilitates enhanced absorption, exciton dissociation, carrier transfer, and thus enhanced photoresponse properties under red light illumination.

## 2. Results and Discussion

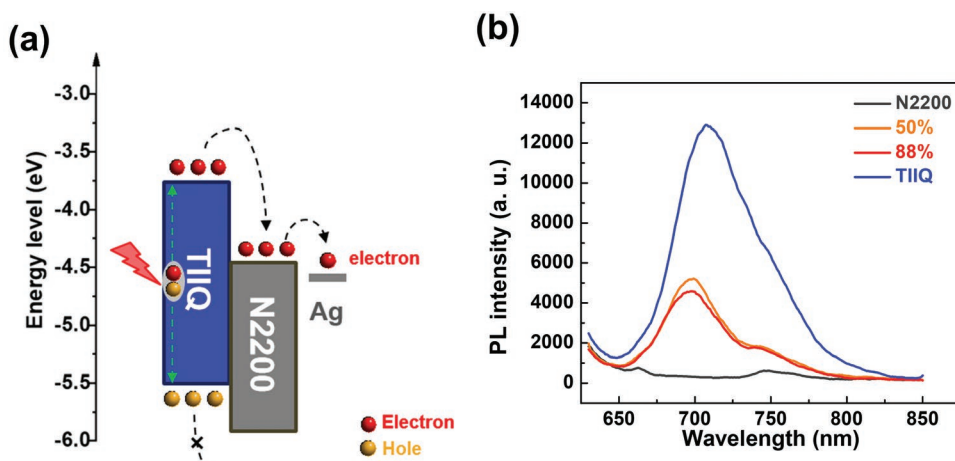
We report on the fabrication and characterization of the n-type semiconducting blends based on N2200 conjugated polymer and TIIQ small molecule (chemical structures presented in

Figure 1a) as the photoactive layer in red light responsive phototransistors. These were fabricated in a bottom-gate top-contact (BGTC) configuration (schematics presented in Figure 1b) onto a Si/SiO<sub>2</sub> substrate by solution shearing the 2 mg mL<sup>-1</sup> solution, comprising pristine N2200 and TIIQ, and 50%/88% TIIQ in the blend system. Figure 1c compares the UV–vis absorption of N2200, TIIQ, and 50%/88% blend films. It is clearly shown that, in comparison with the absorption band of N2200 polymer, ranging from 500 to 800 nm, TIIQ has a strong characteristic peak at 666 nm. Both absorption bands are summarized in Table S2, Supporting Information. These two compounds were found to exhibit the intense absorption in the deep red light region (650–700 nm). The blend films follow the superimposition of the spectrum of the individual N2200 and TIIQ constituents, suggesting that the photoresponse of blend films may be affected by these two compounds. It should also be noted that the stronger absorption at 666 nm in blend films is able to harvest more incident red light photons, which is beneficial for efficient exciton generation in phototransistor devices.

Considering the absorption spectra of N2200:TIIQ blends, red light illuminated on the samples is absorbed by the photoactive layer and thus electron–hole pairs seem to be photogenerated.<sup>[45]</sup> A schematic illustration of energy level alignment between TIIQ and N2200 is illustrated in Figure 2a. The HOMO energy levels ( $E_{\text{HOMO}}$ ) of both solution sheared films was determined via photoelectron (PE) spectroscopy in air after calibration of the onset points.<sup>[46,47]</sup> From linearly extrapolating the onset of PE yield in spectra (Figure S1, Supporting Information), the  $E_{\text{HOMO}}$  of TIIQ and N2200 was found to be  $-5.50$  and  $-5.90$  eV, respectively. The LUMO energy levels ( $E_{\text{LUMO}}$ ) of TIIQ and N2200 are  $-3.75$  and  $-4.45$  eV, respectively, as determined from the difference between the optical bandgap and  $E_{\text{HOMO}}$ . For intrinsic n-channel transport in N2200 polymer, the frontier molecular orbitals become stabilized compared to TIIQ small molecules. In other words, the  $E_{\text{HOMO}}$  of TIIQ features a higher energy level than that of N2200, thereby impeding hole transport from TIIQ. Conversely, N2200 behaves trapping sites in the heterojunction for the driving force of electron transport from LUMO of TIIQ to low-lying LUMO of N2200. This efficient electron transfer of photogenerated electrons was verified by the photoluminescence (PL) spectra of N2200:TIIQ blend



**Figure 1.** a) Molecular structures of organic semiconductor N2200 and TIIQ. b) Schematic representation of N2200:TIIQ blend phototransistor with bottom-gate top-contact architecture under red light illumination. c) UV–vis absorption spectra of N2200, TIIQ, and their blend (50% and 88%) films.



**Figure 2.** a) Energy level diagram of electron transport between TIIQ and N2200. b) Photoluminescence spectra of pristine and N2200:TIIQ blend films at an excitation wavelength of 600 nm.

films. As indicated in Figure 2b, the considerably suppressed PL intensity of blend films compared to pristine TIIQ infers the energetically favorable separation and transfer of photo-generated carriers which can be observed in the heterojunction between TIIQ and N2200.<sup>[48]</sup>

Polarized optical microscope (POM) and atomic force microscope (AFM) analysis was carried out to investigate the microstructures and surface morphologies of pristine and N2200:TIIQ blend films. **Figures 3a** and **b** show the optical and polarized optical micrographs of N2200, 50%/88% blend, and

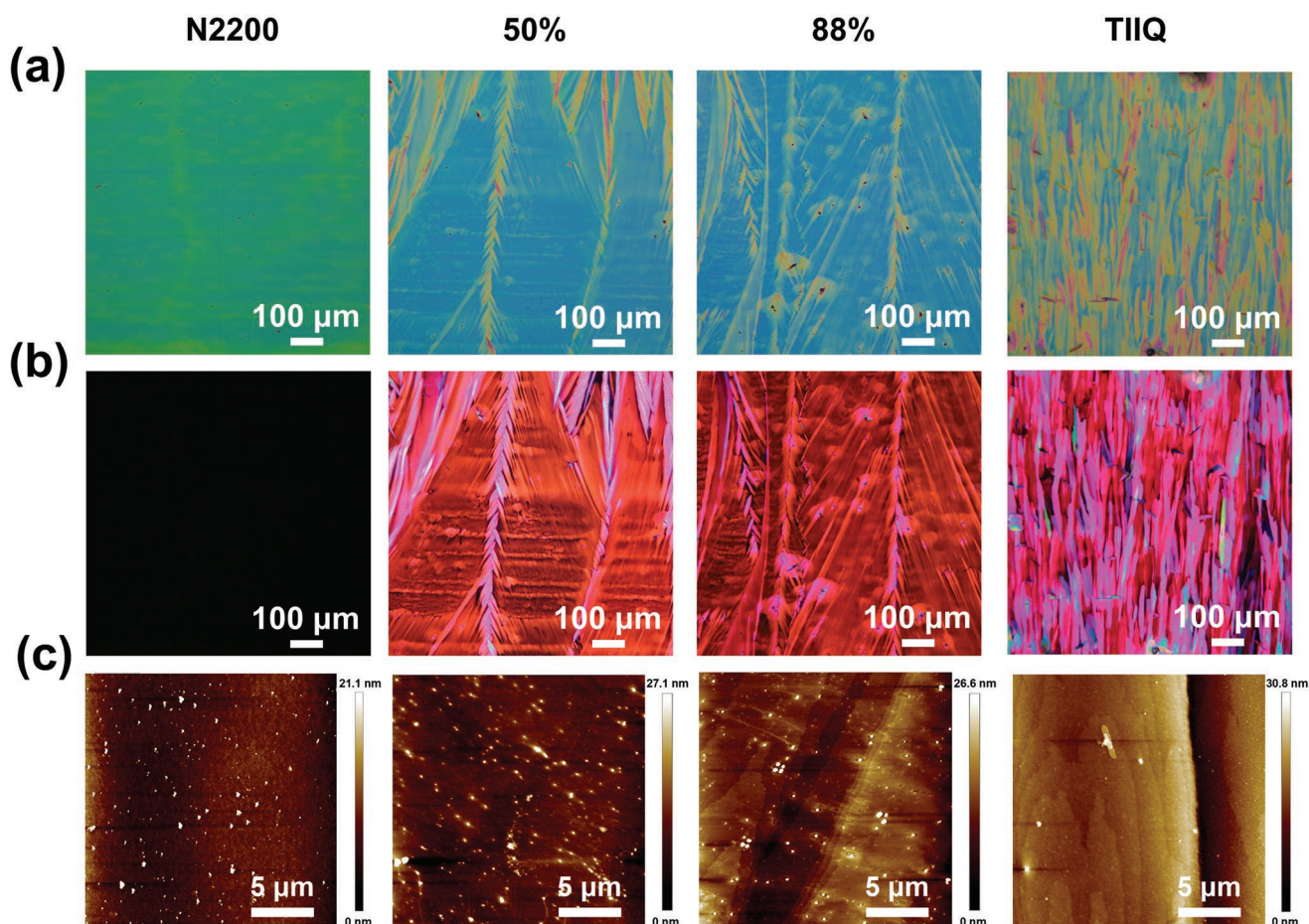


**Figure 3.** a) Optical and b) polarized optical microscopy images and c) AFM topographies for N2200, 50% blend, 88% blend, and TIIQ films.

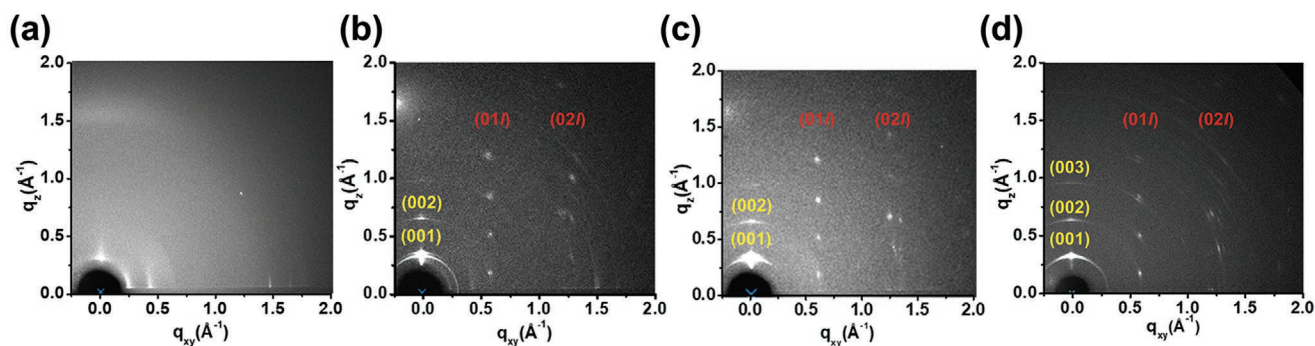


**Figure 4.** 2D GIXRD patterns of solution-sheared a) N2200, b) 50% blend, c) 88% blend, and TIIQ thin films.

TIIQ films, respectively, formed on the self-assembly monolayer treated SiO<sub>2</sub> substrate by solution shearing. The pristine N2200 polymer film exhibits a flat surface with nontextured morphologies, while the pristine TIIQ film images are highly textured and are composed of stripe-like crystals with the preferential orientation along the shearing direction. Similar textured patterns can be seen for the blend films, but with fewer aligned crystals as the fraction of TIIQ decreases, which evidences the unchanged nature of the crystals in the blends during the processing. As shown in the topographic AFM images of Figure 3c, the pristine N2200 and TIIQ films reveal small scattered aggregates and molecule-level terraces on the surface, respectively, and the blend films show both features. As the fraction of TIIQ increases, the surfaces become rougher, which can be evidenced by the increasing root-mean-square roughness from 2.7 to 4.0, 4.3, and 10.4 nm for N2200, 50% blend, 88% blend, and TIIQ, respectively. The rough surface morphology of the blend films from the crystalline domains may contribute to a positive effect on the charge transport property as well as the corresponding photoresponse.<sup>[12,49,50]</sup> In addition, spectroscopic PL signal imaging from the N2200:TIIQ blend films is capable of mapping the film morphological information with micrometer scale spatial distribution. Based on the fitted 128 × 128 mapping spectra, overview pictures of PL intensity distribution of N2200 and TIIQ molecules in the 1 × 1 mm<sup>2</sup> scan area of 88% blend film (derived from the PL emission peak of the pristine N2200:TIIQ with maximum at 699 nm/750 nm; Gaussian fitting function) are shown in Figure S2a,b, Supporting Information, respectively. A comparison between these two figures clearly demonstrates that the N2200 and TIIQ are well distributed over the tested sample area without the presence of oversized aggregates. The correlation of the PL features of these two phases suggests that the heterojunctions are endowing a bicontinuous mixing of the N2200 and TIIQ within the blends.

In addition to surface morphologies, 2D grazing incidence X-ray diffraction (GIXRD) was performed to compare the structures inside the N2200, TIIQ, and blend films. The diffraction patterns are shown in **Figure 4**. A face-on molecular packing can be found for pristine N2200, based on the lamellar diffraction peak visible along the in-plane direction and the peak from  $\pi$ - $\pi$  stacking along the out-of-plane direction (Figure 4a).<sup>[51]</sup> The pristine TIIQ film shows the intensive diffraction patterns at  $q_{xy} = 0.64$  and  $1.28 \text{ \AA}^{-1}$ , corresponding to the (01l) and (02l) planes of the TIIQ crystals (Figure 4d).<sup>[44]</sup> For the blend films, both the N2200 and TIIQ diffraction characteristics

were observed without positional shift. As shown in Figure 4c, the 88% blend film, with a lower N2200 fraction, exhibits a less intense (100) peak of the crystalline N2200 domains. The results indicate that the blends comprise the intact domains formed by the phase separation between N2200 and TIIQ.<sup>[40]</sup> The phenomena observed in GIXRD of the blend films show the same trend as those of the POM/AFM images as well as the absorption/PL spectra. In addition, the TIIQ crystalline correlation lengths ( $L_c$ s) in pristine and 88% blend films were estimated from the (001) diffraction peaks shown in Figure S3, Supporting Information using the Scherrer equation.<sup>[52]</sup> The  $L_c$ s are 31.5 and 26.2 nm for the pristine TIIQ and 88% blend films, respectively, which suggests a relatively smaller N2200 crystallite present in the blend, in line with the POM/AFM images. Therefore, the combination of the phase separation between N2200 and TIIQ and the large TIIQ crystallites in the blends, as compared with the low-crystalline pristine N2200, can contribute to the charge transport and separation.<sup>[53]</sup>

Based on these solution sheared thin film properties, photoelectric characteristics of the BGTC organic phototransistor were evaluated through three-terminal drain current-gate voltage ( $I_d$ - $V_g$ ; transfer curves) and drain current-drain voltage ( $I_d$ - $V_d$ ; output curves) measurement to identify the illumination response for these four photoactive layers. **Figure 5a** shows the transfer curves of the pristine and N2200:TIIQ blend phototransistor during the  $V_g$  sweeping from -40 to 80 V and  $V_d$  bias at 100 V observed in dark and under illumination of various 680 nm red light intensities from 0.03 to 3 mW cm<sup>-2</sup>. In the dark state, all the devices present a typical behavior of n-type channel of field effect transistor and exhibit increased  $I_d$  by the introduction of TIIQ with the extracted saturated mobility of 0.17, 1.18, 1.59, and 2.54 cm<sup>2</sup> V<sup>-1</sup> s<sup>-1</sup> for N2200, 50% and 88% blend, and TIIQ, respectively. It is also noted that the obvious negatively-shifted threshold voltage ( $V_{th}$ ) of 50% and 88% blend as compared with pristine N2200 and TIIQ devices indicates the increase in charge trapping states within the heterointerfaces.<sup>[54]</sup> Under different light conditions, the electrical characteristics of pristine N2200 devices do not change obviously, perhaps due to the limited red light absorption, and there is a small shift (0.34 V) in  $V_{th}$ . On the contrary, the change of photocurrent of blend and TIIQ devices, compared to dark current, becomes more and more obvious and the  $V_{th}$  shifts ( $\Delta V_{th}$ ) more negatively with light intensity increasing under the light illumination, since TIIQ can help to absorb more photons. The electron transfer from TIIQ to N2200, which comes from the

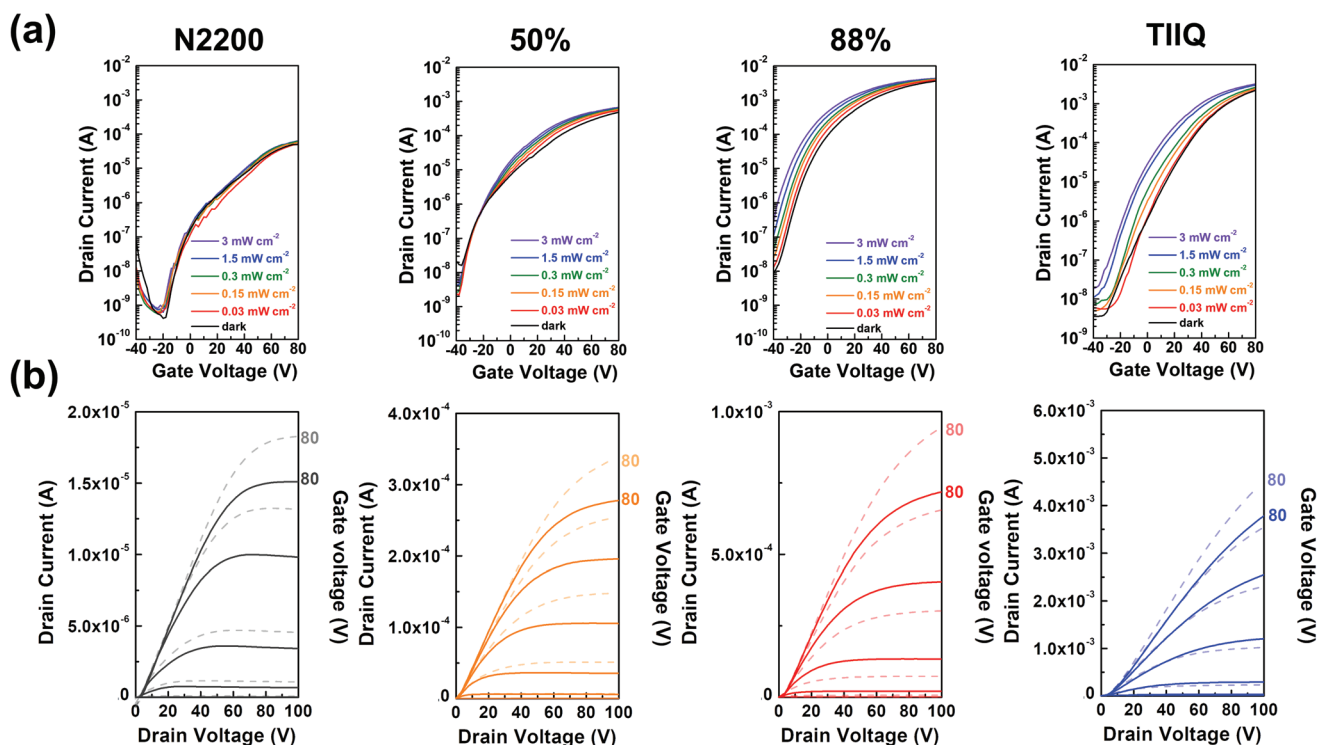


**Figure 5.** Electrical and optoelectrical characteristics of the pristine and N2200:TIIQ blend phototransistor: a) Transfer characteristics measured at  $V_d$  of 100 V in dark and under different illumination intensities in the range of 0.03 to 3  $\text{mW cm}^{-2}$ . b) Output characteristics measured at  $V_g$  of -20, 0, 40, 60, and 80 V in dark and under  $P_{\text{ill}}$  of 3  $\text{mW cm}^{-2}$ .

potential barrier at the heterointerface, ultimately leads to the negative  $\Delta V_{\text{th}}$  and  $I_d$  enhancement of the N2200:TIIQ phototransistor.<sup>[15,55,56]</sup> Figure 5b presents the output curves of the device in the dark and under light illumination of 3  $\text{mW cm}^{-2}$  at different  $V_g$ . The photocurrent increases more significantly in the 88% blend device than in pristine N2200 device, when  $V_g$  increases from 0 to 80 V, which confirms the photogenerated charges in the blend film can be efficiently separated between these two organic semiconductor domains. These traps are gradually populated with inserted TIIQ by photoexcited charges as  $V_g$  increases.<sup>[57]</sup> In order to quantitatively evaluate the performance of pristine and blend films as phototransistors, we calculated the key-of-merits, such as  $R$ , photosensitivity ( $P$ ), and  $D^*$  for red light absorbing photodetector, which can be determined by the following equations:

$$R = \frac{I_{\text{light}} - I_{\text{dark}}}{P_{\text{ill}} A} \quad (1)$$

$$P = \frac{I_{\text{light}} - I_{\text{dark}}}{P_{\text{dark}}} \quad (2)$$

$$D^* = R \left( \frac{A}{2qI_{\text{dark}}} \right)^{1/2} \quad (3)$$

where  $I_{\text{light}}$  and  $I_{\text{dark}}$  are drain current under light illumination and in the dark condition, and  $P_{\text{ill}}$ ,  $A$ , and  $q$  are the incident illumination power density, effective channel area, and charge

of an electron, respectively.<sup>[58,59]</sup> If the shot noise from the dark current is the major contributor to limit the detectivity,  $D^*$  can be expressed as equation (3).<sup>[32]</sup> These key factors of the device under  $P_{\text{ill}}$  of 3, 1.5, 0.3, 0.15, and 0.03  $\text{mW cm}^{-2}$  and bias of  $V_g = 0$  V and  $V_d = 100$  V are exhibited in Table 1. By comparing these values,  $R$  and  $\Delta V_{\text{th}}$ , as a function of  $P_{\text{ill}}$ , are plotted in Figure 6a,b, respectively. Figure 6a shows that  $R$  and  $P_{\text{ill}}$  give an inverse linear relationship in their double logarithmic plot. The observation of decreased  $R$  with increasing  $P_{\text{ill}}$  for all these three devices is probably due to the saturated absorption<sup>[60]</sup> or charge trapping/separation and increased recombination loss<sup>[49,61]</sup> at high  $P_{\text{ill}}$ . Pristine TIIQ device without heterointerface exhibits less  $P_{\text{ill}}$  dependent  $R$  value (slower  $R$  value decrease with increased  $P_{\text{ill}}$ ) as compared with blend one, which may be associated with slow detrapping or recombination process of trapped holes. Under the weak  $P_{\text{ill}}$  of 0.03  $\text{mW cm}^{-2}$ , the N2200, 50% and 88% blend and TIIQ devices reach the maximum

**Table 1.** Summary of photoelectric parameters of phototransistors under 680 nm red light illumination at  $V_g = 0$  and  $V_d = 100$  V.

Compound	$\mu^{\text{eff}}$ [ $\text{cm}^2 \text{V}^{-1} \text{s}^{-1}$ ]	$R$ [ $\text{A W}^{-1}$ ]	$P$	$D^*$ [Jones]
N2200	0.17	0.12	0.16	$9.9 \times 10^9$
50% blend	1.18	136	1.64	$1.8 \times 10^{12}$
88% blend	1.59	4065	3.88	$1.4 \times 10^{13}$
TIIQ	2.54	1848	37.49	$1.2 \times 10^{13}$

<sup>a)</sup> Maximum mobility.

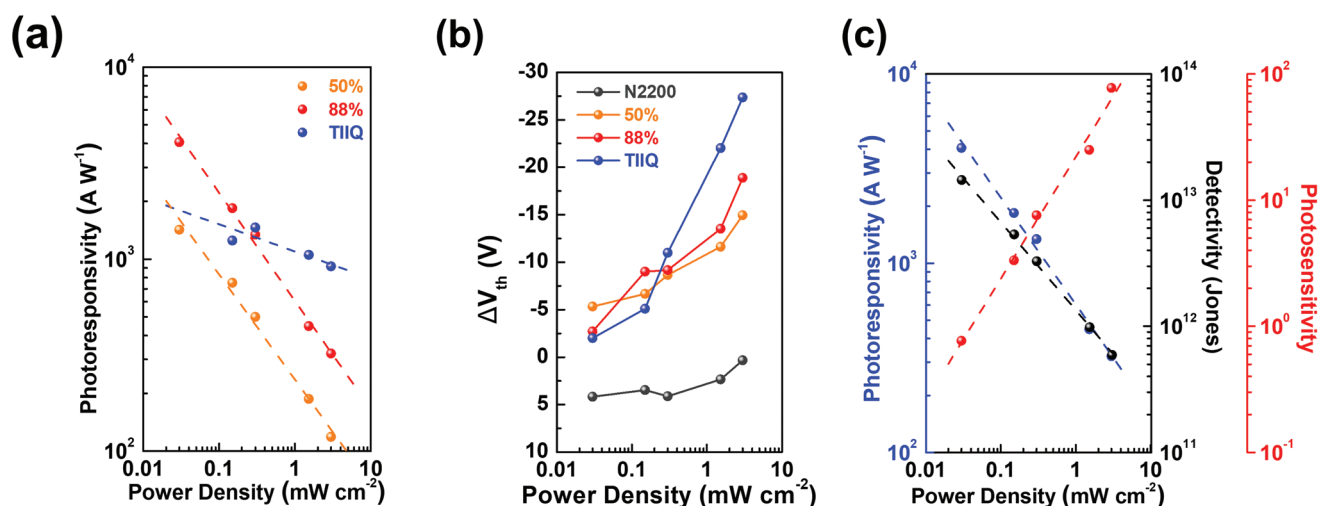


**Figure 6.** Changes in a)  $R$  and b)  $\Delta V_{\text{th}}$  as a function of  $P_{\text{ill}}$  for the pristine and blend organic phototransistors. c)  $R$ ,  $P$ , and  $D^*$  versus  $P_{\text{ill}}$  of the 88% blend device at  $V_g = 0$  and  $V_d = 100$  V.

$R$  values of 0.12, 1.36, 4065, and 1848  $\text{A W}^{-1}$ , respectively. As expected from the absorption characteristics (Figure 1c), the 88% blend device provides a significant response to the red light illumination, due to the enhanced photogenerated carrier formation and their efficient separation,<sup>[62]</sup> which is superior to the previously reported blend red light phototransistor of  $\approx 14 \text{ A W}^{-1}$ .<sup>[40]</sup> Besides, a small  $\Delta V_{\text{th}}$  can be obtained for the pristine N2200 device and the value does not significantly change even under high  $P_{\text{ill}}$ , as shown in Figure 6b, indicating red light photo-insensitivity in N2200. In contrast, the pristine TIIQ and N2200:TIIQ blend devices provide a linear relationship between  $\Delta V_{\text{th}}$  and  $P_{\text{ill}}$ , and the maximum negative  $\Delta V_{\text{th}}$  of 88% blend is  $-18.8$  V at a  $P_{\text{ill}}$  of  $3 \text{ mW cm}^{-2}$ . More details on  $P_{\text{ill}}$  dependent  $R$ ,  $P$ , and  $D^*$  values of the 88% blend device are summarized in Figure 6c. It should be noted that the tendency of  $D^*$  in the higher  $P_{\text{ill}}$  region is a similar trend with  $R$ , while giving the reverse trend for  $P$ . Obviously, in the case of photoactive blend films, a significant enhancement in  $R$ ,  $D^*$ , and  $\Delta V_{\text{th}}$  can be observed as compared to the case of the original N2200 device. The remarkable highest  $D^*$  for the 88% blend device is calculated as  $1.4 \times 10^{13}$  Jones under the  $P_{\text{ill}}$  of  $0.03 \text{ mW cm}^{-2}$ , as well as the highest  $R$ . This can be explained by more significant accumulation of photogenerated electron-hole pairs, high electron mobility (for photo-gain) and charge trapping ability of TIIQ in blends. Therefore, the applied  $V_g$  enhances the charge dissociation and reduces the recombination, demonstrating the more sensitive detection capability of the N2200:TIIQ blend phototransistor when illuminated using red light.

Figure 7a shows the time-dependent photoresponse of N2200:TIIQ blend and pristine TIIQ phototransistors at  $V_g = 0$  and  $V_d = 100$  V, as the red light with  $P_{\text{ill}}$  of  $3 \text{ mW cm}^{-2}$  is turned on and off. Figure 7b displays an example of one switching cycle, and each cycle contains light-on (5 s)/light-off (1 s), light-on (5 s)/light-off (1.5 s)/ $V_g$  bias (20 V, 1 s), and light-on (5 s)/light-off (1.5 s)/ $V_g$  bias (50 V, 1 s) for 50%, 88% blend and pristine TIIQ devices, respectively. It shows that the 50% blend device can be repeatedly and perfectly switched during the alternating illumination and dark conditions. The photocurrent

continuously increases/decreases and the on- and off-current states remain during the repetitive photoswitching, without any applied external  $V_g$ . The rising and falling time, defined as the increased and decreased  $I_{\text{light}}$  between 10% and 90% of the peak value, are found to be 23 and 45 ms, respectively. On the other hand, both the 88% blend and pristine TIIQ devices can be switched on by light illumination, but switched off with the help of resetting the electrical pulse ( $V_g = 20$  V and 50 V for 1 s, respectively) under light-off condition. It should be noted that the incorporation of 88% TIIQ in the blend affects the  $I_{\text{light}}$  evolution versus time, characterized by a slow increase of the red light illuminated  $I_{\text{light}}$  and a noticeable persistent  $I_{\text{light}}$  decay as the device is returned to the dark condition. Similar photoreponse phenomena can be found for the pristine TIIQ device. The delay in  $I_{\text{light}}$  falling may be caused by persistent photoconductivity,<sup>[48,63]</sup> which occurs when the trapped holes remain in the photoactive channel.<sup>[64]</sup> The trapped holes affect the electrical characteristic when the device is not illuminated,<sup>[65]</sup> and a rapid drop of  $I_{\text{light}}$  occurs only when an electrical bias is applied. From the abovementioned photoresponse results, the rising and falling time of 50% blend device can be greatly improved mainly associated with efficient exciton dissociation/hole trapping process to reach steady state upon illumination and whole detrapping in the dark from this heterointerface, respectively. In contrast, an increase in exciton formation and more hole-electron needed to be separated due to increased amounts of red light absorbed TIIQ in 88% blend and pristine TIIQ devices contribute to the sluggish rise/fall response time.<sup>[66]</sup> The release of trapped holes is allowed only at the additional positive  $V_g$  pulse. Especially, the pristine TIIQ device needs more positive the sweep out (50 V) to return back to the initial off current state since more trapped holes need to be detrapped while there is no intrinsic heterointerface to trigger the detrapping process. We also check the transient photoresponse for prolonged period in the 88% blend phototransistor (Figure S4, Supporting Information). In the first 200 s, the  $I_d$  still presents a relative good photoresponse under red light illumination and recovery from electrical bias. After that, it can be found that the  $I_{\text{light}}$  gradually

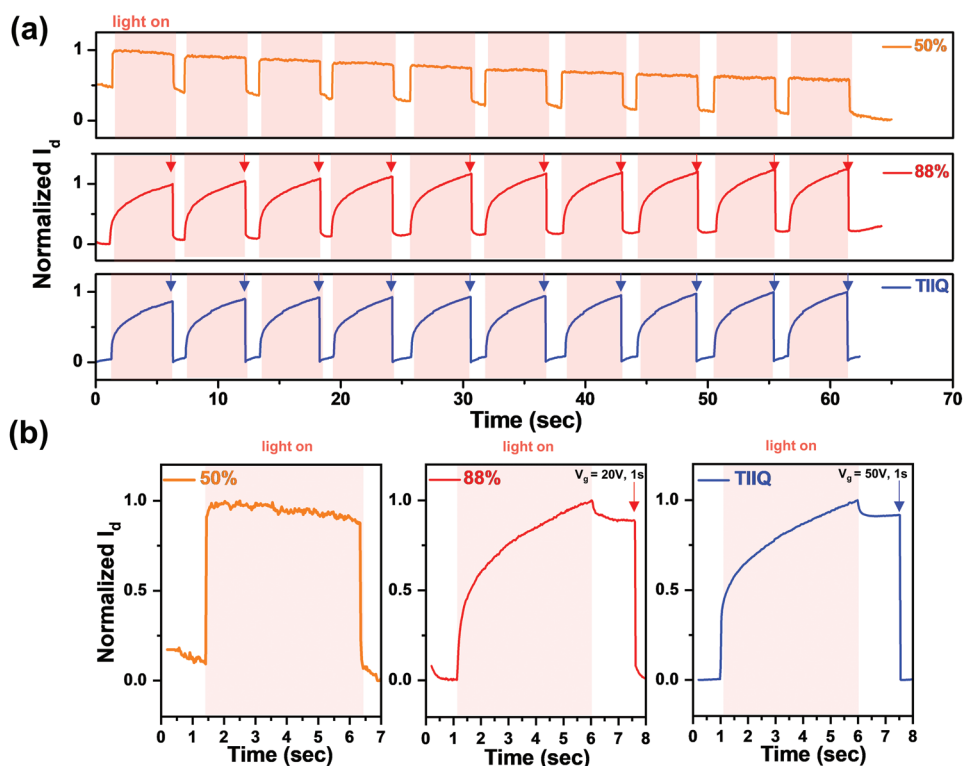


**Figure 7.** a) Transient photoresponse of the 50% blend, 88% blend, and pristine TIIQ devices over time under alternative illumination and dark conditions for ten illumination cycles. (The pink region indicates the device under red light illumination; the arrows in the 88% blend and pristine TIIQ indicate the application of pulsed  $V_g = 20$  and  $50$  V for  $1$  s, respectively). b) An example of one illumination cycle.

decreases, implying the slower rate in both charge trapping and trap-assisted recombination at the later stage. This device may need longer illumination time to reach original on-current state. Even through the decrease in  $I_{light}$  happens, these two distinct on- and off-current states can still be observed for at least  $950$  s. Overall, the N2200:TIIQ blend phototransistor devices presented here exhibited good photoswitching ability upon irradiation with red light and modulated photoelectric response of the device by simply choosing the blends of organic/polymeric semiconductors with suitable composition.

### 3. Conclusion

In conclusion, photomodulation between  $I_{light}$  and  $I_{dark}$  of phototransistors can be achieved through the solution-processable semiconducting blends of N2200 conjugate polymer and TIIQ small molecule. Our results demonstrate that the photoresponse of a N2200:TIIQ blend phototransistor can be tuned by the blend composition and morphologies of the photoactive blend layer. The blends are seen to compromise the enhanced red light absorption and high charge carrier mobility from TIIQ semiconductor and the charge separation between the N2200:TIIQ heterointerface, when compared to the pristine film. Taking advantage of these findings, we have realized a 88% blend reaching high  $\mu$ ,  $R$ , and  $D^*$  values of  $1.59$   $\text{cm}^2$   $\text{V}^{-1}$   $\text{s}^{-1}$ ,  $4065$   $\text{A}$   $\text{W}^{-1}$ , and  $1.4 \times 10^{13}$  Jones, respectively, under red light illumination. In addition, the light-driven current modulation possesses good stability and reproducibility.

Our results demonstrate that the solution-processed N2200:TIIQ blend phototransistor developed in this study provides an effective approach for improved photodetection.

### 4. Experimental Section

**Materials:** N-type blend semiconducting layers based on small molecule semiconductor TIIQ was synthesized according to previously reported procedure,<sup>[44]</sup> whereas n-type conjugated polymer semiconductors N2200 (molecular weight of  $M_n = 150497$  and a polydispersity index of  $1.93$ ) was obtained from Ossila. (2-phenylethyl) trichlorosilane and n-decyltrimethoxysilane were purchased from Gelest and used as a surface modification agent. All the solvents purchased from Sigma-Aldrich were anhydrous grade. All the reagents and commercially available chemicals were used without further purification.

**Phototransistor Fabrication and Measurement:** First, the pure N2200 was dissolved in 1,2-dichlorobenzene with a solid concentration of  $5$   $\text{mg}$   $\text{mL}^{-1}$ . The blend N2200:TIIQ solution (at a weight ratio of 50:50 and 88:12) was mixed at a fixed concentration of  $2$   $\text{mg}$   $\text{mL}^{-1}$  in mixing solvent of 1,2-dichlorobenzene and chloroform (97:3 vol%). Prior to depositing the photoactive blend films, the solutions were stirred on a plate and preheated for  $30$  min at the same temperature during the shearing process. Heavily-doped n-type silicon wafers were used as substrates for phototransistor in bottom-gate geometry. The thermal growth  $300$  nm-thick  $\text{SiO}_2$  layer was used a gate dielectric. The photoactive blend layer was deposited by solution shearing process onto the silane-modified substrates at a shearing rate of  $10$ – $100$   $\mu\text{m}$   $\text{s}^{-1}$  and deposited temperature of  $80$ – $120$   $^\circ\text{C}$ , followed by annealing at  $100$   $^\circ\text{C}$  for  $1$  h under vacuum. The thickness of the obtained films was  $\approx 30$  nm. Finally, the phototransistors were completed by Ag deposition as top-contact electrode ( $\approx 80$  nm thick) via thermal evaporation through the shadow mask with a channel length ( $L$ ) of  $25$   $\mu\text{m}$  and width ( $W$ )

of 1500  $\mu\text{m}$ . The phototransistors were characterized in the dark and under red light irradiation from the top of the sample surface under a nitrogen atmosphere using a Keithley 4200-SCS semiconductor parameter analyzer equipped with 680 nm red light emitting diode source. The incident light intensity was performed at real power intensity of 0.003–3  $\mu\text{W cm}^{-2}$  calibrated using an analogue optical power meter (Newport 1919-R).

## Supporting Information

Supporting Information is available from the Wiley Online Library or from the author.

## Acknowledgements

The authors gratefully acknowledge the funding from the Young Scholar Fellowship Program (Columbus Program) by Ministry of Science and Technology (MOST) in Taiwan, under grant MOST 110-2636-E-002-021. The beamline B13A1/B17A1/B23A1 from the National Synchrotron Radiation Research Center (NSRRC) of Taiwan for providing beamtime is also appreciated.

## Conflict of Interest

The authors declare no conflict of interest.

## Data Availability Statement

The data that support the findings of this study are available from the corresponding author upon reasonable request.

## Keywords

blend films, n-type blends, organic phototransistors, organic semiconductors, red light photodetection

Received: December 6, 2021

Revised: January 29, 2022

Published online: March 25, 2022

- [1] K.-J. Baeg, M. Binda, D. Natali, M. Caironi, Y.-Y. Noh, *Adv. Mater.* **2013**, *25*, 4267.
- [2] B. Lucas, T. Trigaud, C. Videlot-Ackermann, *Polym. Int.* **2012**, *61*, 374.
- [3] Y. Wakayama, R. Hayakawa, H.-S. Seo, *Sci. Technol. Adv. Mater.* **2014**, *15*, 024202.
- [4] C. Wang, X. Zhang, W. Hu, *Chem. Soc. Rev.* **2020**, *49*, 653.
- [5] H. Dong, H. Zhu, Q. Meng, X. Gong, W. Hu, *Chem. Soc. Rev.* **2012**, *41*, 1754.
- [6] X. Huang, D. Ji, H. Fuchs, W. Hu, T. Li, *ChemPhotoChem* **2020**, *4*, 9.
- [7] X. Wei, W. Zhang, G. Yu, *Adv. Funct. Mater.* **2021**, *31*, 2010979.
- [8] P. Gu, Y. Yao, L. Feng, S. Niu, H. Dong, *Polym. Chem.* **2015**, *6*, 7933.
- [9] H. Ren, J.-D. Chen, Y.-Q. Li, J.-X. Tang, *Adv. Sci.* **2020**, *8*, 2002418.
- [10] D. P. Karothu, G. Dushaq, E. Ahmed, L. Catalano, M. Rasras, P. Naumov, *Angew. Chem., Int. Ed.* **2021**, *60*, 26151.
- [11] G. Wang, K. Huang, Z. Liu, Y. Du, X. Wang, H. Lu, G. Zhang, L. Qiu, *ACS Appl. Mater. Interfaces* **2018**, *10*, 36177.
- [12] M. J. Kim, S. Choi, M. Lee, H. Heo, Y. Lee, J. H. Cho, B. Kim, *ACS Appl. Mater. Interfaces* **2017**, *9*, 19011.
- [13] J. H. Kim, S. Oh, S. K. Park, S. Y. Park, *Adv. Electron. Mater.* **2019**, *5*, 1900478.
- [14] S. K. Samanta, I. Song, J. H. Yoo, J. H. Oh, *ACS Appl. Mater. Interfaces* **2018**, *10*, 32444.
- [15] J. H. Kim, M. W. Choi, S. Y. Kim, S. Jung, Y. S. Choi, S. Y. Park, *Adv. Opt. Mater.* **2020**, *8*, 2000695.
- [16] X. Gong, M. Tong, Y. Xia, W. Cai, J. S. Moon, Y. Cao, G. Yu, C.-L. Shieh, B. Nilsson, A. J. Heeger, *Science* **2009**, *325*, 1665.
- [17] Y. Yao, Y. Liang, V. Shrotriya, S. Xiao, L. Yu, Y. Yang, *Adv. Mater.* **2007**, *19*, 3979.
- [18] Y. Xu, Q. Lin, *Appl. Phys. Rev.* **2020**, *7*, 011315.
- [19] Y. Pan, G. Yu, *Chem. Mater.* **2021**, *33*, 2229.
- [20] H. Han, S. Nam, J. Seo, C. Lee, H. Kim, D. D. Bradley, C. S. Ha, Y. Kim, *Sci. Rep.* **2015**, *5*, 16457.
- [21] S. Nam, H. Han, J. Seo, M. Song, H. Kim, T. D. Anthopoulos, I. McCulloch, D. D. C. Bradley, Y. Kim, *Adv. Electron. Mater.* **2017**, *2*, 1600264.
- [22] S. Nam, H. Kim, D. D. C. Bradley, Y. Kim, *Org. Electron.* **2016**, *39*, 199.
- [23] H. Han, S. Nam, J. Seo, J. Jeong, H. Kim, D. D. C. Bradley, Y. Kim, *IEEE J. Sel. Top. Quantum Electron.* **2015**, *22*, 147.
- [24] H. Han, C. Lee, H. Kim, J. Seo, M. Song, S. Nam, Y. Kim, *ACS Appl. Mater. Interfaces* **2017**, *9*, 628.
- [25] C. Lee, J. Kim, Y. Moon, D. Kim, D.-I. Song, H. Kim, Y. Kim, *Asian J. Org. Chem.* **2018**, *7*, 2330.
- [26] C. Lee, J. Kim, Y. Moon, D. Kim, H. Han, H. Kim, Y. Kim, *Dyes Pigm.* **2018**, *156*, 219.
- [27] X. Ren, F. Yang, X. Gao, S. Cheng, X. Zhang, H. Dong, W. Hu, *Adv. Energy Mater.* **2018**, *8*, 1801003.
- [28] N. Marjanović, T. B. Singh, G. Dennler, S. Günes, H. Neugebauer, N. S. Sariciftci, R. Schwödiauer, S. Bauer, *Org. Electron.* **2006**, *7*, 188.
- [29] C. T. Herrera, M. J. Hong, J. G. Labram, *ACS Appl. Electron. Mater.* **2020**, *2*, 2257.
- [30] R. Shidachi, N. Matsuhisa, P. Zalar, P. C. Y. Chow, H. Jinno, T. Yokota, T. Someya, *Phys. Status Solidi RRL* **2018**, *12*, 1700400.
- [31] S. Nam, H. Hwang, H. Kim, Y. Kim, *Mol. Cryst. Liq. Cryst.* **2010**, *519*, 260.
- [32] M. Shou, Q. Zhang, H. Li, S. Xiong, B. Hu, J. Zhou, N. Zheng, Z. Xie, L. Ying, L. Liu, *Adv. Opt. Mater.* **2021**, *9*, 2002031.
- [33] T. Han, L. Sun, Q. Feng, K. Cao, S. Ding, G. Jin, C. Jiang, X. Huang, *J. Mater. Chem. C* **2020**, *8*, 12284.
- [34] L. Ma, B. Chen, Y. Guo, Y. Liang, D. Zeng, X. Zhan, Y. Liu, X. Chen, *J. Mater. Chem. C* **2018**, *6*, 13049.
- [35] H. Xu, J. Liu, J. Zhang, G. Zhou, N. Luo, N. Zhao, *Adv. Mater.* **2017**, *29*, 1700975.
- [36] H. Xu, J. Li, B. H. K. Leung, C. C. Y. Poon, B. S. Ong, Y. Zhanga, N. Zhao, *Nanoscale* **2013**, *5*, 11850.
- [37] T. Han, M. Shou, L. Liu, Z. Xie, L. Ying, C. Jiang, H. Wang, M. Yao, H. Deng, G. Jin, J. Chen, Y. Ma, *J. Mater. Chem. C* **2019**, *7*, 4725.
- [38] S. Cook, H. Ohkita, Y. Kim, J. J. Benson-Smith, D. D. C. Bradley, J. R. Durrant, *Chem. Phys. Lett.* **2007**, *445*, 276.
- [39] A. Armin, R. D. Jansen-van Vuuren, N. Kopidakis, P. L. Burn, P. Meredith, *Nat. Commun.* **2015**, *6*, 6343.
- [40] S. Nam, J. Seo, H. Han, H. Kim, D. D. C. Bradley, Y. Kim, *ACS Appl. Mater. Interfaces* **2017**, *9*, 14983.
- [41] X. Liu, H. Wang, T. Yang, W. Zhang, I.-F. Hsieh, S. Z. Cheng, X. Gong, *Org. Electron.* **2012**, *13*, 2929.
- [42] Y. S. Rim, Y. M. Yang, S.-H. Bae, H. Chen, C. Li, M. S. Goorsky, Y. Yang, *Adv. Mater.* **2015**, *27*, 6885.
- [43] J. Han, J. Wang, M. Yang, X. Kong, X. Chen, Z. Huang, H. Guo, J. Gou, S. Tao, Z. Liu, *Adv. Mater.* **2018**, *30*, 1804020.



- [44] A. Velusamy, C.-H. Yu, S. N. Afraj, C.-C. Lin, W.-Y. Lo, C.-J. Yeh, Y.-W. Wu, H.-C. Hsieh, J. Chen, G.-H. Lee, S.-H. Tung, C.-L. Liu, M.-C. Chen, A. Facchetti, *Adv. Sci.* **2021**, *8*, 2002930.
- [45] J. Zhong, X. Wu, S. Lan, Y. Fang, H. Chen, T. Guo, *ACS Photonics* **2018**, *5*, 3712.
- [46] H. Kim, M. Shin, Y. Kim, *Macromol. Res.* **2009**, *17*, 445.
- [47] S. Nam, M. Shin, H. Kim, C.-S. Ha, M. Ree, Y. Kim, *Adv. Funct. Mater.* **2011**, *21*, 4527.
- [48] K. Shi, R. Jin, S. Huang, H. Lei, P. Dai, D. Chi, W. Zhang, G. Yu, *J. Mater. Chem. C* **2021**, *9*, 322.
- [49] F. Huang, X. Wang, K. Xu, Y. Liang, Y. Peng, G. Liu, *J. Mater. Chem. C* **2018**, *6*, 8804.
- [50] F. Huang, X. Wang, K. Xu, Y. Liang, Y. Peng, G. Liu, *J. Mater. Chem. C* **2018**, *6*, 8803.
- [51] M. Pandey, N. Kumari, S. Nagamatsu, S. S. Pandey, *J. Mater. Chem. C* **2019**, *7*, 13323.
- [52] F.-J. Lin, H.-H. Chen, Y.-T. Tao, *ACS Appl. Mater. Interfaces* **2019**, *11*, 10801.
- [53] H. Wang, Z. Zhang, X. Liu, S. Qu, S. Guang, Z. Ye, J. Yu, W. Tang, *Chem. Eng. J.* **2021**, *413*, 127444.
- [54] J. Belasco, S. K. Mohapatra, Y. Zhang, S. Barlow, S. R. Marder, A. Kahn, *Appl. Phys. Lett.* **2014**, *105*, 063301.
- [55] D. Kufer, G. Konstantatos, *ACS Photonics* **2016**, *3*, 2197.
- [56] D. Ji, T. Li, J. Liu, S. Amirjalayer, M. Zhong, Z.-Y. Zhang, X. Huang, Z. Wei, H. Dong, W. Hu, H. Fuchs, *Nat. Commun.* **2019**, *10*, 12.
- [57] Y. Qin, S. Long, Q. He, H. Dong, G. Jian, Y. Zhang, X. Hou, P. Tan, Z. Zhang, Y. Lu, C. Shan, J. Wang, W. Hu, H. Lv, Q. Liu, M. Liu, *Adv. Electron. Mater.* **2019**, *5*, 1900389.
- [58] Y. Guo, G. Yu, Y. Liu, *Adv. Mater.* **2010**, *22*, 4427.
- [59] X. Wu, B. Zhou, J. Zhou, Y. Chen, Y. Chu, J. Huang, *Small* **2018**, *14*, 1800527.
- [60] W. J. Yu, Y. Liu, H. Zhou, A. Yin, Z. Li, Y. Huang, X. Duan, *Nat. Nanotechnol.* **2013**, *8*, 952.
- [61] P. Agnihotri, P. Dhakras, J. U. Lee, *Nano Lett.* **2016**, *16*, 4355.
- [62] W. Rekab, M.-A. Stoeckel, M. E. Gemayel, M. Gobbi, E. Orgiu, P. Samori, *ACS Appl. Mater. Interfaces* **2016**, *8*, 9829.
- [63] H. Wang, C. Cheng, L. Zhang, H. Liu, Y. Zhao, Y. Guo, W. Hu, G. Yu, Y. Liu, *Adv. Mater.* **2014**, *26*, 4683.
- [64] R. Jia, X. Wu, W. Deng, X. Zhang, L. Huang, K. Niu, L. Chi, J. Jie, *Adv. Funct. Mater.* **2019**, *29*, 1905657.
- [65] D. Ljubic, W. Liu, C. E. González-Espinoza, N.-X. Hu, Y. Wu, S. Zhu, *Adv. Electron. Mater.* **2017**, *3*, 1700284.
- [66] P. C. Chow, N. Matsuhisa, P. Zalar, M. Koizumi, T. Yokota, T. Someya, *Nat. Commun.* **2018**, *9*, 4546.